Raman Spectroscopy Follows Time-Dependent Changes in T Lymphocytes Isolated from Spleen of Endotoxemic Mice

Anuradha Ramoji, Oleg Ryabchykov, Kerstin Galler, Astrid Tannert, Robby Markwart, Robert P. Requardt, Ignacio Rubio, Michael Bauer, Thomas Bocklitz, Jürgen Popp and Ute Neugebauer

ImmunoHorizons 2019, 3 (2) 45-60
doi: https://doi.org/10.4049/immunohorizons.1800059
http://www.immunohorizons.org/content/3/2/45

ImmunoHorizons is an open access journal published by
The American Association of Immunologists, Inc.,
1451 Rockville Pike, Suite 650, Rockville, MD 20852

ISSN 2573-7732.

ImmunoHorizons

RESEARCH ARTICLE

Adaptive Immunity

Raman Spectroscopy Follows Time-Dependent Changes in T Lymphocytes Isolated from Spleen of Endotoxemic Mice

Anuradha Ramoji,[*,†,‡] Oleg Ryabchykov,[†,‡] Kerstin Galler,[*,†] Astrid Tannert,[*,†,§] Robby Markwart,[*] Robert P. Requardt,[*] Ignacio Rubio,[*,¶] Michael Bauer,[*,§,¶] Thomas Bocklitz,[†,‡] Jürgen Popp,[*,†,‡,§,‖] and Ute Neugebauer[*,†,‡,§,‖]

*Center for Sepsis Control and Care, Jena University Hospital, 07747 Jena, Germany; [†]Leibniz Institute of Photonic Technology Jena, 07745 Jena, Germany; [‡]Institute of Physical Chemistry and Abbe Center of Photonics, Friedrich Schiller University, 07743 Jena, Germany; [§]Jena Biophotonics and Imaging Laboratory, 07745 Jena, Germany; [¶]Department of Anesthesiology and Intensive Care, Jena University Hospital, 07747 Jena, Germany; and [‖]InfectoGnostics Research Campus Jena, 07743 Jena, Germany

ABSTRACT

T lymphocytes (T cells) are highly specialized members of the adaptive immune system and hold the key to the understanding the hosts' response toward invading pathogen or pathogen-associated molecular patterns such as LPS. In this study, noninvasive Raman spectroscopy is presented as a label-free method to follow LPS-induced changes in splenic T cells during acute and postacute inflammatory phases (1, 4, 10, and 30 d) with a special focus on $CD4^+$ and $CD8^+$ T cells of endotoxemic C57BL/6 mice. Raman spectral analysis reveals highest chemical differences between $CD4^+$ and $CD8^+$ T cells originating from the control and LPS-treated mice during acute inflammation, and the differences are visible up to 10 d after the LPS insult. In the postacute phase, $CD4^+$ and $CD8^+$ T cells from treated and untreated mice could not be differentiated anymore, suggesting that T cells largely regained their original status. In sum, the biological information obtained from Raman spectra agrees with immunological readouts demonstrating that Raman spectroscopy is a well-suited, label-free method for following splenic T cell activation in systemic inflammation from acute to postacute phases. The method can also be applied to directly study tissue sections as is demonstrated for spleen tissue one day after LPS insult. *ImmunoHorizons*, 2019, 3: 45–60.

INTRODUCTION

T cells have been widely studied as an important component of adaptive immunity (1–3). T cells originate from bone marrow and migrate to thymus for maturation. The majority of T cells resides in the spleen, a lymphoid organ accounting for 25% of total body lymphocytes (3).

T cells emerge from the thymus with specific genomic DNA sequences that dictate the surface TCRs through which the cellular activation process is mediated (4). Naive T cells circulate mainly through the lymphatic system and through the spleen. During their circulation, T cell clones that come across their cognate Ags presented on APCs become activated via their TCRs, expand clonally, and lead the host's body response against the infectious pathogen (4–6). The T cell activation process is an indirect process. T cells require APCs for their activation (7–9). LPS triggers inflammatory response of cytokine release, reactive oxygen species formation, and

Received for publication August 28, 2018. Accepted for publication January 17, 2019.

Address correspondence and reprint requests to: Prof. Ute Neugebauer, Center for Sepsis Control and Care, Jena University Hospital, Am Klinikum 1, 07747 Jena, Germany. E-mail address: ute.neugebauer@med.uni-jena.de

ORCIDs: 0000-0003-2723-6614 (A.R.); 0000-0002-4655-8080 (O.R.); 0000-0002-1521-3514 (M.B.); 0000-0003-2778-6624 (T.B.).

This work was supported by grants from the European Union via the European Union project HemoSpec (CN 611682), the Federal Ministry of Education and Research via the Integrated Research and Treatment Center (Center for Sepsis Control and Care) (FKZ 01EO1502), and the Deutsche Forschungsgemeinschaft within Research Group FOR1738 via the Jena Biophotonic and Imaging Laboratory (FKZ PO633/29-1, BA 1601/10-1). Furthermore, the work was performed within the Research Campus InfectoGnostics (FKZ 13GW0096F), the Leibniz ScienceCampus InfectoOptics (SAS-2015-HKI-LWC), and the COST (European Cooperation in Science and Technology) Action Raman-Based Applications for Clinical Diagnostics, Raman4Clinics (BM 1401). The publication of this article was supported by the Open Access Fund of the Leibniz Association.

Abbreviations used in this article: AUC, area under the curve; LD, linear discriminant; LDA, LD analysis; NA, numerical aperture; PC, principal component; PCA, PC analysis; ROC, receiver operating characteristic; SNIP, sensitive nonlinear iterative peak.

The online version of this article contains supplemental material.

https://doi.org/10.4049/immunohorizons.1800059

various mediator responses and mobilizes the immune cells, in particular the T cells.

T cells are investigated for the relative ratio of their subtypes, for their surface receptor expression that may reflect priming, activation, tolerance or exhaustion, and for their functional response to the stimulations performed via various stimulation modes. Most commonly employed methods include but are not limited to flow cytometry, immunohistochemistry, immunophenotyping, and gene expression analysis. All these methods target the understanding of intracellular biochemical changes and surface modifications. However, despite all these well-established approaches, T cell activation modes and their functionality are not fully understood, and many aspects related to T cell dysfunction are still debated (7, 8, 10–12). Further, by conventional immunological readouts it is hard to capture long-term changes associated with inflammation within the lymphocytes.

With regard to endotoxemia and systemic infections, such as found in the case of sepsis, accumulating evidence supports the concept that T cells lapse into a protracted immune-suppressed, anergy-like state where they are functionally inactivated (8, 10, 11). In the state of endotoxin (7, 8) and/or infection-related shock leading to sepsis, T cell functionality gets altered at multiple levels (9, 13, 14). For a better understanding of the changes occurring within the T cells that can be applied for targeted drug therapy and for adoptive T cell transfer therapeutic development, there is a need for fast, cost-effective, and label-free methods of T cell phenotyping. Such noninvasive methods can provide information about T cell functional status in their native state in a non-destructive and label-free manner without much alteration of the cells during the investigation.

Raman spectroscopy is an emerging method in biomedical research that allows investigating biochemical features of the cells in a nondestructive and label-free manner, which in turn enables discrimination of different cell types as well as their functional states. In Raman spectroscopy, laser light is scattered upon interacting with the biomolecules, and the inelastically scattered light contains information about the molecular vibrations that are very specific to the molecule. Hence, complex information about the cell and its activation status is captured by the Raman spectra. Accordingly, Raman spectroscopy has been applied to characterize leukocytes for single-cell analysis (15, 16), to follow cellular activation status in cell lines (15, 17, 18), cell–drug, and cell–cell interactions (18–20) as well as differentiation of cell types (20–22). In the current study we have explored the potential of Raman spectroscopy for analysis of the T cells isolated from the mice spleen and for the investigation of spleen tissue from mice after LPS insult (1). Our findings show that Raman spectroscopy allows the capture of the activation pattern of the T cell subtypes $CD4^+$ and $CD8^+$ isolated from the spleen of mice suffering from acute and postacute inflammation. Importantly, we document that Raman spectroscopy results are in agreement with the results obtained from traditional immunology (23), as they highlighted the greatest differences in the T cell's phenotype after 4 d post–LPS treatment rather than at longer postacute stages.

MATERIALS AND METHODS

Mouse strains

Protocols related to mouse handling and concerning ethical permission have been reported previously (23). From the same study, mice cells and spleen tissue samples were received. In brief, Black 6 mice were allowed to adapt to laboratory conditions and to artificial day and night cycle for at least 4 d. Laboratory temperature was maintained at 23°C, and humidity was kept between 60 and 70%. The mice received standard mouse diet. Experiments performed in the Jena University Hospital were conducted in accordance with German legislation on protection of animals and with permission from the regional animal welfare committee of Thuringia (permit Tierversuchsantrag (animal test request) Registration no. 02-046/11) (23).

LPS-induced inflammation mouse model

Details of the mice experiments have been described in the previous publication (23). In brief, C57BL/6 murine endotoxemia model was used in which mice were injected with LPS i.p. (9 to 11 mg/kg body weight) or 0.9% saline water (for control mice). Mice were sacrificed at a specified period of time: 1, 4, 10, or 30 d (see Fig. 1) after the LPS insult. The clinical scores of the mice after LPS insult have been shown in our previous publication (23).

Raman spectroscopic investigation of T cells

T cell isolation from mouse spleen and sample preparation. T cells were isolated from pooled spleens as described previously (23). Briefly, spleens were placed on a 70-μm cell strainer and gently squashed with a plunger. Cells were washed with washing buffer (PBS; Biochrom) supplemented with 0.5% BSA (PAA Laboratories), and 2 mM EDTA (AppliChem). Contaminating erythrocytes were removed by lysis. Cells were washed and $CD4^+$ T cell and $CD8^+$ T cell subsets were purified using automated negative magnetic sorting (autoMACS Pro system; Miltenyi Biotech) using $CD4^+$ and $CD8^+$ standard isolation kit protocols (Miltenyi Biotech order no. 130-104-454 and 130-096-495). Briefly, T cells pellet was resuspended in 40 μl of buffer per 10^7 cells, and 10 μl of Biotin-Ab Cocktail was added. Cells were incubated for 5 min at 4°C followed by 30 μl of buffer and 20 μl of Anti-Biotin MicroBeads and further incubation for 10 min at 4°C. Total volume of the cell suspension was adjusted to 500 μl and, using autoMACS Pro Separator, a negatively selected enriched fraction of $CD4^+$ and $CD8^+$ T cells was obtained. Throughout the isolation procedure the cells were maintained at a temperature of 4°C. The purity of T cell preparations was assessed by flow cytometry on a FACS Calibur (BD Pharmingen) using anti-human CD4-PE (clone MEM-241, ImmunoTools) and anti-human CD8-allophycocyanin (clone MEM-31, ImmunoTools). Data analysis was performed with FlowJo software (Tree Star). Purified $CD4^+$ T cells or $CD8^+$ T cells were discriminated from magnetic purification beads via forward scatter/side scatter blotting followed by quantification of CD4-/CD8-positive cells in bivariate $CD4^+/CD8^+$ or univariate histogram blotting (Supplemental Fig. 2). For Raman analysis, purified $CD4^+$ and $CD8^+$ T cells were

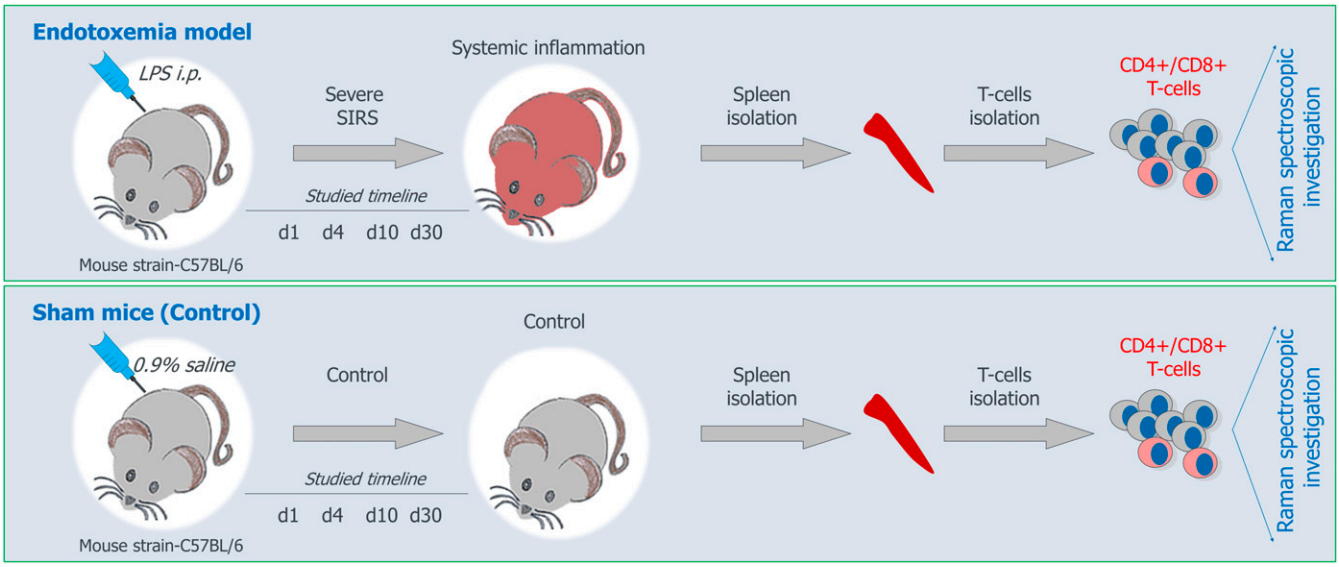

FIGURE 1. Experimental design for in vivo LPS challenge of C57BL/6 mice and disease index post–LPS insult.

fixed with 4% formaldehyde (Carl Roth) for 10 min on ice. Chemical fixation is a common procedure applied for Raman spectroscopic imaging of cells and tissue to preserve the information relevant to cellular activation state as well as to maintain the structural integrity of the cells (24, 25). Afterwards the cells were washed with washing buffer (PBS + 0.5% BSA + 2 mM EDTA) and followed by washing with 0.9% sodium chloride (NaCl; Merck) solution. Two different methods were employed to coat the cells on the slides; 1) the cells (1×10^6 cells) were resuspended in 100 μl of 0.9% NaCl solution and coated onto CaF_2 (Crystal) slide using cytospin (Shandon Cytospin 3 Cytocentrifuge; Thermo Fisher Scientific) (6 min, 300 g), 2) the cells (1×10^6 cells) were embedded in 100 μl of 0.75% of alginate (Sigma-Aldrich) solution on CaF_2 slides to allow for measurement in suspension. The cells were immobilized by polymerization of alginate using 0.5 M calcium chloride solution (Sigma-Aldrich) followed by a washing step using PBS. Both methods are commonly used to investigate single cells by means of Raman spectroscopy with the latter one becoming slightly more established (25). After preparation, cells were stored at 4°C and measured within 4 h.

Four different time points after LPS treatment of mice, namely, 1, 4, 10, and 30 d, have been investigated in this study. For each time point a minimum of three biological replicate experiments were performed. At each time point and for each biological replicate 9 to 12 mice were used, and T cells were isolated from pooled spleens (23).

Raman spectroscopy. Raman spectra of T cells were recorded with an upright micro-Raman setup (CRM 300; WITec) equipped with a 300 grooves per mm grating blazed at 750 nm. A diode laser with a wavelength of 785 nm was used for excitation. The 180°-backscattered light from the sample was guided through a fiber 100 μm in diameter and detected with a back-illuminated deep depletion charge coupled device camera (DU401A BR-DD, ANDOR, 1024 × 128 pixels) cooled down to −60°C. For the two different sample preparation methods, two different measurement modes were employed: cytospin-coated cells were measured in air (T cells 10 d post–LPS treatment and T cells batch 3 of 4 d post–LPS treatment), whereas cells embedded in alginate were immersed in sterile-filtered (0.2-μm filters) tap water (1, 4, and 30 d post–LPS treatment). Raman spectra acquisition of T cells in air and in water results in vibrational spectra capturing similar information of the cellular biochemical composition. When measured in water additional Raman peaks of water are observed (OH stretching at 3200 cm^{-1} and OH deformation at 1600 cm^{-1}) (Supplemental Fig. 1A, 1C). Differences in the spectral background can be corrected by spectral preprocessing (Supplemental Fig. 1B). Thus, differences in the sample preparation method had no influence on the Raman spectroscopy outcome (i.e., spectroscopic differentiation of the different time points when individual sampling points are compared). Raman maps of randomly selected, individual cells were recorded in area scanning mode with a step size of 0.3 μm and integration time per spectrum 0.5 to 2 s. A white light image of an exemplary cell is depicted in the inset of Supplemental Fig. 1C. For the dry cells, 100×/numerical aperture (NA) 0.9 (Carl Zeiss Microscopy) objective was used. For the samples measured by immersing in water, a 60×/NA 1.0 water immersion objective (Nikon) has been used. The laser power before the objective was 200 mW. Approximatively 400 to 600 spectra per cell region were obtained. The biological experiments were repeated minimum three times (Supplemental Table IA).

Spectroscopic investigation of spleen tissue

Sample preparation. Mice were injected i.p. with LPS or 0.9% saline water and sacrificed after 24 h. Spleens were collected and immediately frozen in liquid nitrogen. Spleen samples were stored

https://doi.org/10.4049/immunohorizons.1800059

at −80°C until further use. Cryoslices of the samples were cut in a cryostat (Leica CM3050 S; Leica Biosystems) at a temperature range between −19 and −23°C. Tissue slices for Raman measurements and subsequent immunofluorescence staining were cut at a thickness of 10 μm and transferred on to CaF_2 slides. Three slices were cut per sample for Raman measurements. After Raman measurements the tissue slices were subjected to immunofluorescence staining.

Raman measurements. Spleen tissue slices were cut 1 to 6 d prior to Raman measurements and stored at −20°C until use. The tissue slices were thawed and dried on CaF_2 slides shortly before the measurement. Raman spectra of the tissue slices were recorded with an upright micro-Raman setup (CRM 300; WITec) equipped with a 600 grooves per mm grating blazed at 500 nm. Because excitation with 785 nm yielded a high fluorescence background from spleen tissue sections, a frequency-doubled Nd-YAG laser with a wavelength of 532 nm was used for excitation. The 180°-backscattered light from the sample was guided through a fiber, 50 μm in diameter and detected with a back illuminated deep depletion charge coupled device camera (DU401A BV-532, ANDOR, 1024 × 127 pixels) cooled down to −60°C. The Raman spectra of the tissue sections in air were recorded in area scanning mode from an area of 33 × 33 μm with a step size of 3 μm and 1 s integration time per spectrum using a 100×/NA 0.75 objective (Carl Zeiss Microscopy) and 15 mW of laser power before objective. This objective was chosen to enable Raman spectroscopic imaging of the rough (in micrometer range) tissue surface with an upright microscope. Spleen was collected from a total of eight mice from three independent biological experiments.

Immunofluorescence staining. After Raman measurement the tissue slices were fixed to the CaF_2 slides by acetone (Carl Roth) and permeabilized with Tween-20 (Carl Roth). The labeling procedure started with a blocking step with blocking reagent (Life Technologies). T cells were labeled by a rat anti-CD3 (1:50; AbD Serotec). It was detected by a donkey anti-rat Alexa Fluor 555 (1:400; Abcam). B cells were labeled by a donkey anti-mouse IgG Alexa Fluor 647 (1:200; Abcam). Ab dilutions were prepared in blocking reagent. Between the incubation steps, the samples were rinsed with PBS (Biochrom) containing 0.1% Tween-20. Finally, the samples were embedded in antifading medium (Vectashield; Linaris).

Fluorescence images were acquired using a laser scanning microscope (LSM 510 META; Carl Zeiss). In total, eight mice spleens were used (four controls: A, B, C, and D; four LPS treated: E, F, G, and H). From each mouse, three spleen tissue slices and a minimum of four different positions were imaged using 40×/0.8 Zeiss objective, resulting in 61 spleen tissue images from control mice and 48 spleen tissue images from LPS-treated mice. The following lasers, beam splitters, and filters were used for fluorescence excitation and emission detection: Alexa Fluor 555: HeNe laser 543 nm, main beam splitter 405/488/543, secondary beam splitter 490, bandpass 560–615; Alexa Fluor 647: HeNe laser 633 nm, main beam splitter UV/488/543/633, no emission filter, but the META detector allowing to detect in a narrow emission range.

Statistical data analysis

Preprocessing and statistical analysis of Raman data were carried out with GNU R (26). The Raman spectra preprocessing involves spectra background correction using the sensitive nonlinear iterative peak (SNIP) clipping algorithm (27) and vector normalization.

For *k*-means cluster analysis of T cells, the spectra were processed to remove cosmic spikes and background corrected using SNIP clipping algorithm. Raman fingerprint region (600 to 1800 cm^{-1}) was used for analysis, and the noncellular regions were removed by setting spectral intensity threshold for the Raman band at 1450 cm^{-1}, arising due to CH_2CH_3 deformation of proteins, lipids, and carbohydrates. The *k*-means algorithm was executed to find four different clusters of spectra for each time point common to all the cells for a given time point and ten different clusters of spectra common to all the spleen tissue sections recovered from spleen of sham- and LPS-treated animals. The *k*-means cluster image has been plotted using false-color, and the cluster scores contributing to each cluster have been displayed on the right side of the *k*-means cluster image. The color of the *k*-means cluster spectra corresponds to the respective color of the cluster shown in the images.

T cell analysis. For analysis of the T lymphocyte splenocytes, additional preprocessing steps were involved; every measurement provided a Raman map containing spectra of the cell area and also the spectra collected from noncell area. For reliable analysis, the spectra from the noncell area have to be removed. This noncellular background was detected by integrating the intensity in the region 1100–1500 cm^{-1} of the background-corrected Raman spectra, and the noncellular background was removed. The Raman spectra collected from the cellular region were averaged to obtain averaged Raman spectra per cell. These average spectra were preprocessed; wavenumber axis was calibrated using 4-acetamidophenol spectrum as a standard reference (28), which was measured every time prior to data acquisition. After wavenumber calibration, the spectra were baseline corrected using asymmetric least squares smoothing (29), spectral range from 600 to 1800 cm^{-1} was selected, and spectra were vector normalized. A classification model using linear discriminant (LD) analysis (LDA) was built. Separate models were built for $CD4^+$ T cells and $CD8^+$ T cells to analyze performance of the individual subpopulations of T cells during the induced endotoxin shock.

To avoid model overfitting, a dimensional reduction by principal component (PC) analysis (PCA) was performed prior to LDA. Apart from data reduction PCA has other applications such as outlier detection and selection of important variables related to sample class differences. PCA uses linear combination of the variables of the data and explains the variance by forming PCs. The first few PCs capture the largest variance present within the data, and the last few PCs capture small variances. LDA allows data projection into a vector space from where classification information can be extracted. Further, through LDA sample features can be extracted by maximizing variance between the sample class and minimizing variance within the class using Fisher criterion.

In the current analysis of the T cells, the first 10 PCs that allowed covering more than 95% of data variance for Raman spectra of T cells were used to build the LDA classification model. Individual classification models between the control and treated groups were built separately for 1, 4, 10, and 30 d post–LPS insult time points. To analyze individual subpopulations of T cells during the induced endotoxin shock, we additionally constructed binary classification models for $CD4^+$ T cells and for $CD8^+$ T cells. Each time point includes a minimum of three different biological replicates. The details of number of biological replicates, mice per experiment, and number of T cells investigated along with the total number of Raman spectra recorded have been described in Supplemental Table IA. To evaluate the performance of classifications, receiver operating characteristic (ROC) curves were generated using posterior probabilities predicted by leave-one-cell-out cross-validation of the PCA-LDA models. Area under the curve (AUC) was used as the metric to estimate performance of the classifications. The maximal possible value of AUC is 1 and represents a perfect classification. In contrast, AUC around 0.5 indicates that the classes cannot be distinguished by the model.

Spleen tissues analysis. The preprocessed Raman spectra of spleen tissue sections were also analyzed using LDA. Prior to LDA, PCA was carried out. For the spleen tissue analysis the first seven PCs were used to build the LDA classification model. Raman spectral region 600–1800 cm^{-1} has been used for model building. Spleen tissue analysis was done using three biological replicates (Supplemental Table IB).

The area covered with B cells and T cells was estimated from the fluorescence images of spleen tissue sections stained with an Alexa Fluor 555–labeled Ab binding to T cells and an Alexa Fluor 647–labeled Ab directed against B cells using Fiji (30). A threshold was determined for each channel showing the fluorescence of T cells but omitting any background fluorescence to generate binary images. Subsequently, the number of fluorescent pixels was summed up and related to the total number of image pixels, giving the percentage of the image covered with the respective cell type marker. To evaluate changes in the proportion of B cells and T cells in the investigated mice, the ratio of the areas covered with the respective fluorescence marker was calculated. The analysis of the fluorescence images was done for whole tissue images and only for the Raman-scanned regions.

RESULTS

$CD4^+$ and $CD8^+$ T cell analysis

The T cells samples from endotoxemic mice used in the current study were investigated for their functional properties, which have been reported elsewhere (23). In that study it could be shown that the T cell–mediated immune response and cytokine release were unaltered during postacute inflammation stages. It was noticed that the mice suffered from lymphopenia because of systemic inflammation induced by LPS. Especially the T cell subpopulation $CD4^+$ decreased compared with the $CD8^+$ cell population upon LPS stimulation (23, 31). The surviving mice regained their body weight, albeit not completely, and the clinical severity reduced after 5 d post–LPS treatment (23). It was observed that 10 d post–LPS treatment, clinical markers in plasma for tissue damage (32) such as lactate dehydrogenase, glutamate pyruvate transaminase, and glutamate oxaloacetate transaminase were absent, indicating that the mice eventually recovered from the LPS insult.

Raman spectral analysis. To gain insight into the chemical changes occurring within the splenocytes, $CD4^+$ and $CD8^+$ T cells were isolated from spleen of sham mice and LPS-treated mice (Fig. 1). The purity of the $CD4^+$ and $CD8^+$ T cell preparations was ascertained using flow cytometry analyses and routinely lay in the range between 85 and 92% (see Supplemental Fig. 2) (23). Isolated T cells were subjected to Raman spectroscopic imaging 1, 4, 10, and 30 d post–LPS treatment. Further, by employing *k*-means clustering, Raman cluster image of representative cells were generated to visualize dominating spectra present within the cells. The *k*-means cluster algorithm was performed to obtain four different clusters common to all the cells for individual time point. The *k*-means cluster image (Fig. 2A) and the cluster spectra (Fig. 2B) mainly show contribution from cell nucleus. False-color Raman *k*-means cluster images revealed a round nucleus at all time points for all treatment conditions (Fig. 2). Thus, morphological features were not considered any further, but one averaged spectrum per cell was used for subsequent data analysis. Mean Raman spectra of combined $CD4^+CD8^+$ T cells for all the four time points after LPS treatment along with the controls are shown in Fig. 3A. Lymphocytes have a narrow rim of cytoplasm and a large nucleus (33), as can be visualized from Fig. 2. Indeed, the majority of spectral contribution comes from the nucleus (20). Mean Raman spectra of the individual subtypes $CD4^+$ T cells and $CD8^+$ T cells are shown in Fig. 3B and 3C, respectively. Differences in the mean spectra of T cells from sham mice and LPS-insulted mice are subtle and hard to follow by eye. To visualize the differences, Raman spectra of T cells belonging to the LPS-treated mice were subtracted from Raman spectra of T cells belonging to the sham mice. The difference Raman spectra for $CD4^+CD8^+$ T cells, only for $CD4^+$ T cells, and only for $CD8^+$ T cells subpopulations are shown in Fig. 3D–F, respectively. In the subtracted Raman spectra subtle differences present between the T cells of control, and the endotoxemic mice are marked at the corresponding Raman peak positions. Each of these Raman peaks can be assigned to different chemical moieties. For example, Raman peaks appearing between 780–800 cm^{-1} and ~1071 cm^{-1} arise due to vibration of the phosphate backbone of the nucleic acids (20). Raman peaks around 1640–1686 cm^{-1} and ~1242 cm^{-1} belong to the amide I and amide III vibrations of proteins (34, 35). The significance of the particular biomolecules' contribution can be judged based on the relative intensity of the corresponding Raman peak.

As a response to T cell stimulation, major transcriptional activity begins within the nucleus (36), an effect that manifests in the difference Raman spectra of T cells upon LPS stimulation for 4 d. Accordingly, relatively strong changes are detected in the Raman band at ~795 cm^{-1}, arising from the nucleus moiety (18, 33), which can be assigned to phosphate backbone vibration (15, 35, 37). At

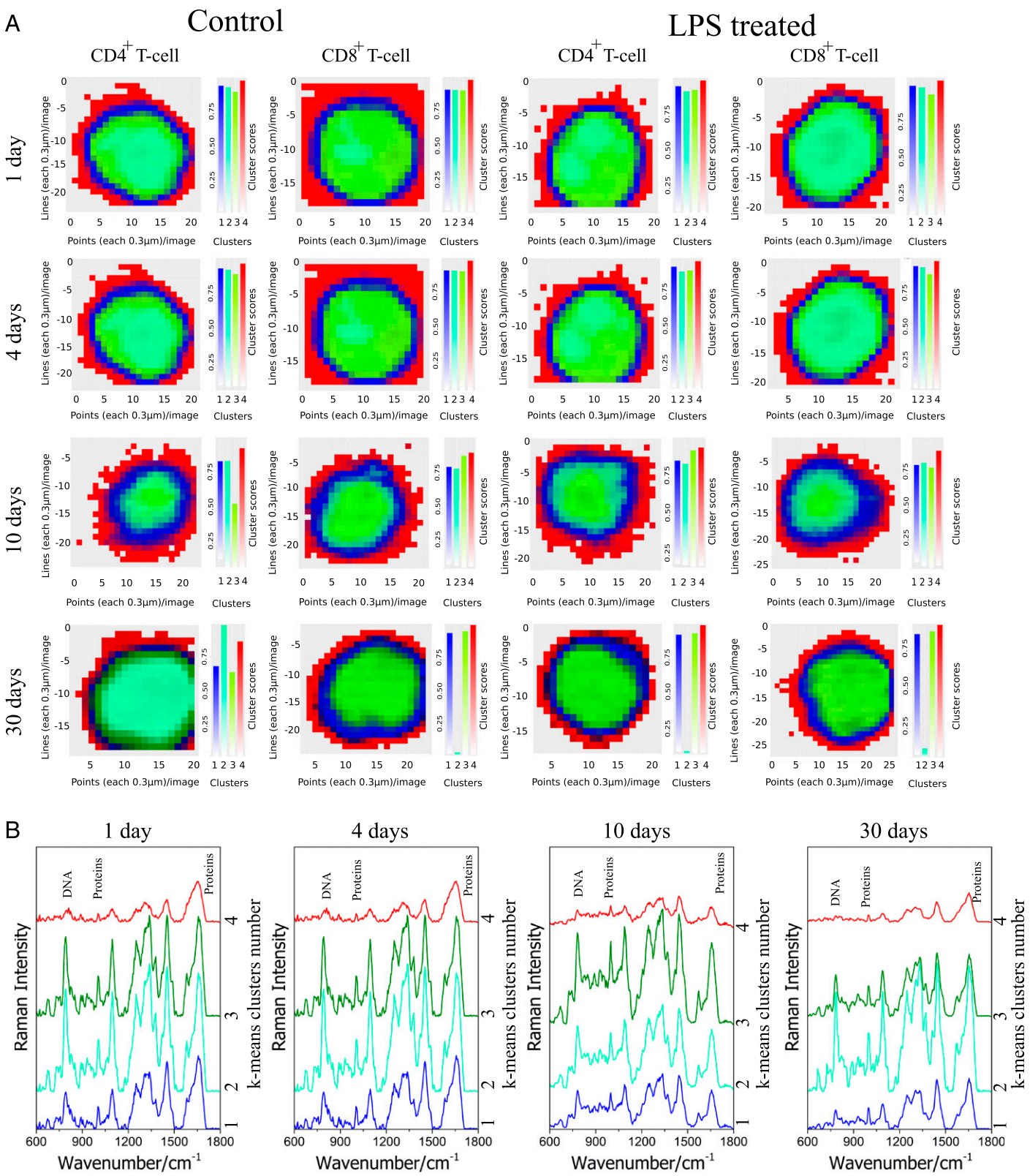

FIGURE 2. False-color Raman images of CD4⁺T cells and CD8⁺ T cells from control and LPS-treated animals after day 1, 4, 10, and 30 obtained by *k*-means cluster analysis.

(**A**) Representative false-color Raman images of CD4⁺ T cells and CD8⁺ T cells from control and LPS-treated animals after day 1, 4, 10, and 30 obtained by applying *k*-means clustering method. The x-axis and y-axis show step size (0.3 μm) used for Raman imaging. The **(Continued)**

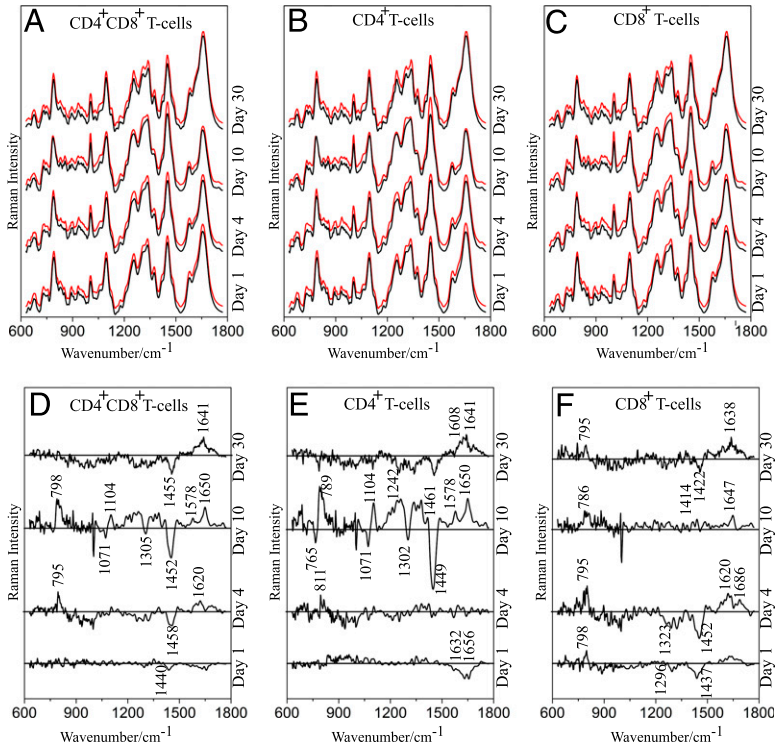

FIGURE 3. Mean and difference Raman spectra of T cells isolated from spleen of sham mice and endotoxemic mice for time points 1, 4, 10, and 30 d.

Top row: mean Raman spectra of (**A**) $CD4^+CD8^+$ T cells, (**B**) $CD4^+$ T cells, and (**C**) $CD8^+$ T cells isolated from spleen of sham C57BL/6 mice and LPS-insulted C57BL/6 mice (time point of LPS insult is shown on right axis). Bottom row: difference Raman spectra between (**D**) $CD4^+CD8^+$ T cells, (**E**) $CD4^+$ T cells, and (**F**) $CD8^+$ T cells from sham mice (spectra in black) and LPS-insulted mice (spectra in red). Negative peaks belong to LPS-treated cells, and positive peaks belong to healthy cells. The spectra are shifted in y-axis for clarity. For each time point, pooled spleen obtained from 9 to 12 mice (both male and female) per condition have been used (see Supplemental Table IA). A minimum of three biological repetition and Raman spectroscopic investigations were done for each time point (see Supplemental Table IA). T cells were isolated, and $CD4^+$ T cells and $CD8^+$ T cells were purified using automated negative magnetic-assisted cell sorting using standard isolation kit.

30 d post-LPS, however, this effect vanishes for $CD4^+$ T cells (Fig. 3E) A closer look at the Raman spectra of $CD4^+$ T cells reveals changes in the Raman peak intensity at 789 cm^{-1} being prominent for day 10 post–LPS stimulation. The variation in the nucleotide conformation changes observed in the Raman spectral region 600–800 cm^{-1} is more pronounced in the $CD4^+$ T cells compared with $CD8^+$ T cells (33). From the difference Raman spectra, the changes in the nuclear composition of the $CD8^+$ T cells are visible at 1, 4, 10, and still weakly 30 d after LPS insult. Further, for day 10 post–LPS treatment, the amide I protein vibration within $CD4^+$ T cells and $CD8^+$ T cells are observed at 1650 cm^{-1} (amide I, β sheet), and for $CD8^+$ T cells, at 4 d post–LPS treatment the amide I vibration is observed at 1620 cm^{-1} (amide I, α helix). The shift in the amide I vibrations observed between 4 and 10 d after LPS treatment is indicative of protein with different structural arrangements within the activated $CD8^+$ T cells. Other Raman vibrations differing between the splenocytes from sham mice and LPS-triggered mice are observed around 1071 cm^{-1} (DNA backbone), 1104 cm^{-1} (glycoproteins), and 1455 cm^{-1} (proteins and lipids) (17, 37–39).

Raman spectroscopy model for T cells. A unifying Raman model built for each LPS stimulation time point separately is shown in Fig. 4A for the $CD4^+CD8^+$ T cells. Separate Raman models built for $CD4^+$ T cells and for $CD8^+$ T cells are shown in Fig. 4B and 4C, respectively. The data for splenocytes of sham mice and

k-means algorithm was executed to find four different clusters of spectra for each time point in the cells recovered from spleen of control and LPS-treated animals. The four clusters are represented by blue, cyan, green, and red color in the image. Blue cluster represents the narrow cytoplasm region of the T cell, cyan and green cluster highlight the nucleus, and red cluster is a mixture of the outer parts of the cell and remaining background contributions. The contribution of each cluster has been represented on right side of individual cells as cluster scores. (**B**) Corresponding Raman spectra of the four clusters obtained from *k*-means analysis using the same color code as in (A).

https://doi.org/10.4049/immunohorizons.1800059

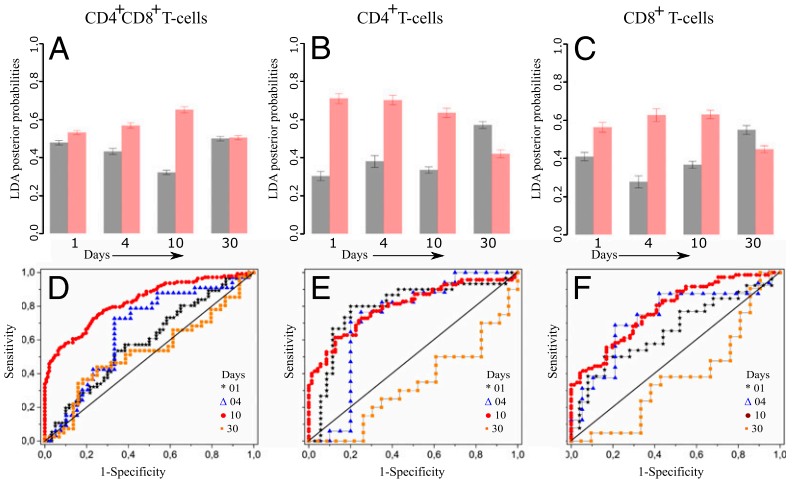

FIGURE 4. PCA-LDA of Raman spectra of T cells isolated from spleen of sham mice and endotoxemic mice for time points 1, 4, 10 and 30 d. Top row: Raman model using PCA-LDA for (**A**) $CD4^+CD8^+$ T cells, (**B**) $CD4^+$ T cells, and (**C**) $CD8^+$ T cells isolated from spleen of sham C57BL/6 mice and LPS-insulted C57BL/6 mice (time point of LPS insult is shown on x-axis). In the bar plots, the bar represents mean along with the SE; black and red bars represent respective control and LPS group. Bottom row: ROC curve for (**D**) $CD4^+CD8^+$ T cells, (**E**) $CD4^+$ T cells, and (**F**) $CD8^+$ T cells from sham mice and LPS-insulted mice. For each time point, pooled spleen obtained from 9 to 12 mice (both male and female) per condition has been used (see Supplemental Table IB). At least three biological repetition and Raman spectroscopic investigations were done for each time point (see Supplemental Table IB). T cells were isolated, and $CD4^+$ T cells and $CD8^+$ T cells were purified using automated negative magnetic-assisted cell sorting using standard isolation kit.

LPS-treated mice are shown as bar plot diagram. As seen from Fig. 4A, T cells from LPS-treated mice are distinct from the controls 1, 4, and 10 d after the insult, whereas no separation is observed for 30 d post-LPS. When the Raman model is built separately for $CD4^+$ (Fig. 4B) and $CD8^+$ T cells (Fig. 4C), more subtle differences show up. For the $CD4^+$ T cells, differences are apparent for 1 d, reach a maximum for 4 d, and are still detectable 10 d post-LPS. However, in $CD4^+$ T cells from 30 d post-LPS, the difference between control and LPS groups are largely lost. In the case of $CD8^+$ T cells, differences between groups start to appear on 1 d post-LPS, the differences are highest 4 d post–LPS treatment and are much lower at 10 d after LPS treatment, and the effect is not detectable at 30 d post-LPS.

The separation discussed above between cells from control mice and LPS-treated mice can be further visualized from the ROC curve (Fig. 4D, 4E) and AUC given in Table I. The AUC for $CD4^+$ and $CD8^+$ T cells when analyzed together is higher for day 10 post-LPS, pointing to the presence of high biochemical difference between the control cells and cells from endotoxemia. There is also fair separation for 4 d post-LPS with AUC of 0.66 (Table I), whereas the samples from 30 d post-LPS show hardly any difference. ROC curve analysis of the $CD4^+$ T lymphocyte population shows higher discrimination of cells from treated and untreated mice at the earlier analyzed three time points post-LPS treatment (1, 4, and 10 d). For the $CD8^+$ T lymphocyte populations, ROC curve test shows similar results. The immunological readouts for day 10 post–LPS treatment published previously (23) showed only differences in number and ratios of T cell populations but no functional differences to be present. However, Raman spectroscopy is based on single-cell analysis and is capable of capturing minute differences present between control and activated T cells. This is the probable explanation for the highest AUCs for $CD4^+$ T cells and $CD8^+$ T cells after 10 d of LPS treatment. The PCA-LDA can be summarized as following: when individual T cell subpopulations are analyzed, the cellular difference starts to appear 1 d after LPS treatment and continues up to 10 d. For the mice that survived for 30 d, the chemical differences in the lymphocyte subpopulations between LPS-treated mice and the controls are very small. By analyzing both $CD4^+$ T cells and $CD8^+$ T cells together as one cell population (T lymphocytes), the cellular difference for 1 d after LPS treatment starts to appear already as concluded above and can be interpreted from the Raman difference spectra shown in Fig. 3D and 3E. However, the difference between T cells from control and LPS-treated mice for other time points is not so pronounced when both cell populations are analyzed together in comparison with when $CD4^+$ T cells and $CD8^+$ T cells populations are analyzed separately. This effect is probably due to the small differences present within individual cell populations that are averaged out when both subpopulations are analyzed together.

Spleen tissue analysis

Raman spectroscopy. To explore further the potential of Raman spectroscopy for direct analysis of tissue samples and to obtain inflammation relevant information, spleen tissue sections obtained from control mice and LPS-treated mice 1 d post–LPS treatment were investigated. The mean Raman spectra of the spleen tissue from sham mice and LPS-treated mice (Fig. 5A) show typical Raman spectral profiles of a tissue as reported in the literature (34, 40, 41). All spectra show Raman vibrational bands attributable

TABLE I. The AUC of the ROC for respective time points

Post–LPS Insult Time Points (d)	Symbol Used for Illustration in Fig. 4	Area under the ROC Curve		
		$CD4^+CD8^+$ T Cells	$CD4^+$ T Cells	$CD8^+$ T Cells
1	* 01	0.59	0.79	0.66
4	Δ 04	0.66	0.72	0.73
10	● 10	0.83	0.80	0.78
30	■ 30	0.53	0.34	0.38

to nucleic acid, protein, tissue resident erythrocyte–related hemoglobin (Hb), and lipids. The difference spectrum shown in Fig. 5A reveals fine changes between spleen tissue of treated and untreated mice. Differences are mainly from Raman vibrations of lipids, proteins, nucleic acids, and Hb or heme moieties. The respective Raman peak positions being 757 cm^{-1} (Hb), 785 cm^{-1} (DNA), 998 cm^{-1} (proteins), 1127 cm^{-1} (lipids), 1177 cm^{-1} (proteins), 1220 cm^{-1} (proteins), 1349 cm^{-1} (Hb), 1558 cm^{-1} (Hb), and 1590 cm^{-1} (nucleic acids) (42, 43). A classification model using PCA-LDA was built in an attempt to distinguish treated and nontreated mice groups and extract the chemical differences present between the two groups. An independent set of spectra was used for prediction of the treatment group. The score plot of PCA-LDA shown as histogram plot in Fig. 5B indicates the possibility to separate tissue sections from the control mice from those tissue sections originating from LPS-treated mice with an accuracy of 68%. This marks a similar accuracy when compared with the splenocytes differentiation model of joint $CD4^+CD8^+$ cells at day 1 (Table I). In the LD histogram plot (Fig. 5B), Raman spectra from control mice are found at positive LD score values, whereas LPS-treated tissue spectra are assigned to negative LD score values. The respective LD coefficient (Fig. 5A) reveals the spectral differences used by the PCA-LDA model for the differentiation of spleen tissue of treated and nontreated mice. Correlation of score values with the LD coefficient supports a relative higher abundance of structurally oriented proteins with β-sheet structure from the amide I band around 1666 cm^{-1} and amide III vibrational band around 1241 cm^{-1} as well as higher cellular DNA content (1489 and 788 cm^{-1}, 730 and 1328 cm^{-1}) in the control mice tissue. In contrast, in samples from LPS-treated mice, the amide I peak shifts toward lower wavenumber (1642 cm^{-1}), indicative of modified protein structure having more α-helix structure. Higher nucleic acids content in samples from LPS-treated mice can be concluded from the appearance of a negative LD coefficient around 1590 cm^{-1} (Fig. 5A). Additional Raman vibrations arising due to lipids (1127 cm^{-1}) and heme/cytochrome-c moiety (1169 and 1546 cm^{-1}) show up in the LD coefficient (Fig. 5A) (38, 44–46). The contribution from nucleic acid and Hb can be further visualized from

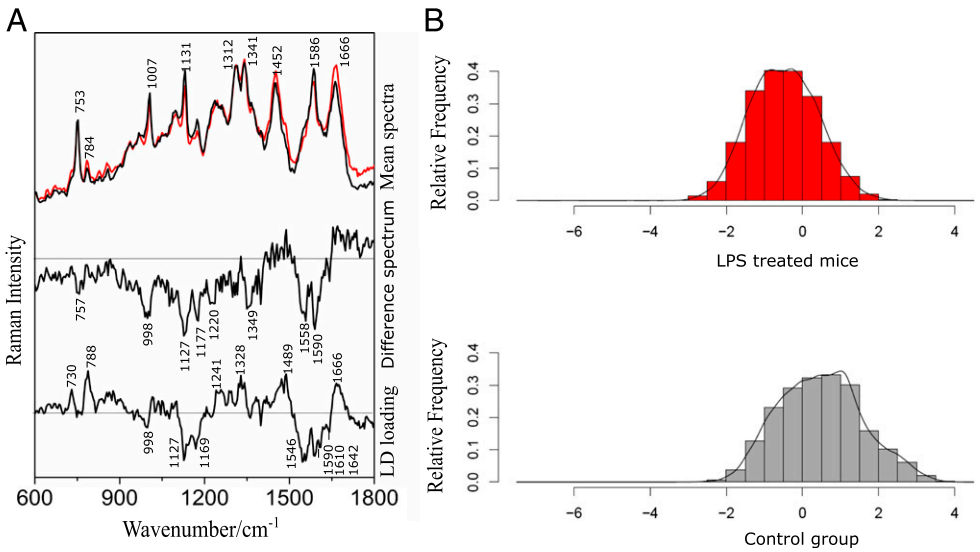

FIGURE 5. Mean and difference Raman spectra of spleen tissue from endotoxemic mice and sham mice and PCA-LDA.
(**A**) Mean Raman spectra of spleen tissue of sham C57BL/6 mice and C57BL/6 mice 1 d post–LPS treatment, difference spectrum between control and LPS-treated mice spleen tissue (label on right y-axis), and loading of PCA-LDA model for spleen tissue section differentiation of control and LPS-treated mice (label on right y-axis). (**B**) PCA-LDA histogram plot. The biological experiments were repeated four times; in each repetition one mouse per condition was used (in total four mice per condition; both female and male mice were used) (see Supplemental Table IB). Raman spectroscopic investigation was performed on three different days. Three tissue slices were investigated per spleen. Analysis has been done on pooled samples.

https://doi.org/10.4049/immunohorizons.1800059

k-means cluster spectra shown in Fig. 6B. The *k*-means cluster algorithm was performed to obtain ten different clusters common to all the tissue sections. The *k*-means cluster image (Fig. 6A) and the cluster spectra (Fig. 6B) mainly show contribution from cell nucleus, Hb, and proteins.

To visualize the major splenocyte distribution and their influence on the classification of the treated and nontreated mice, tissue sections were stained with fluorescently labeled Abs for T cells and B cells after Raman imaging. In Fig. 7, fluorescence and bright-field images of spleen tissue sections are shown for a sham mouse (Fig. 7A, 7B) and for an LPS-treated mouse (Fig. 7C, 7D). Correlation of the Raman-mapped area with the corresponding fluorescence image was enabled by a laser-induced cross-mark on the samples with high laser power as used in previous tissue analysis (47). Judged by the fluorescence images, no tissue damage was introduced by Raman imaging. The ratios of T cells to B cells for all the mice together were calculated 1) for only Raman-mapped regions (Fig. 8A, 8B) and 2) for entire fluorescence images (Fig. 8C, 8D). Relative percentages of T cells to B cells for the sham mouse and LPS-treated mouse are displayed in the form of a pie chart. The ratio of T cells to B cells for individual mice where calculated and are displayed as a bar graph in Fig. 8E and 8F. From

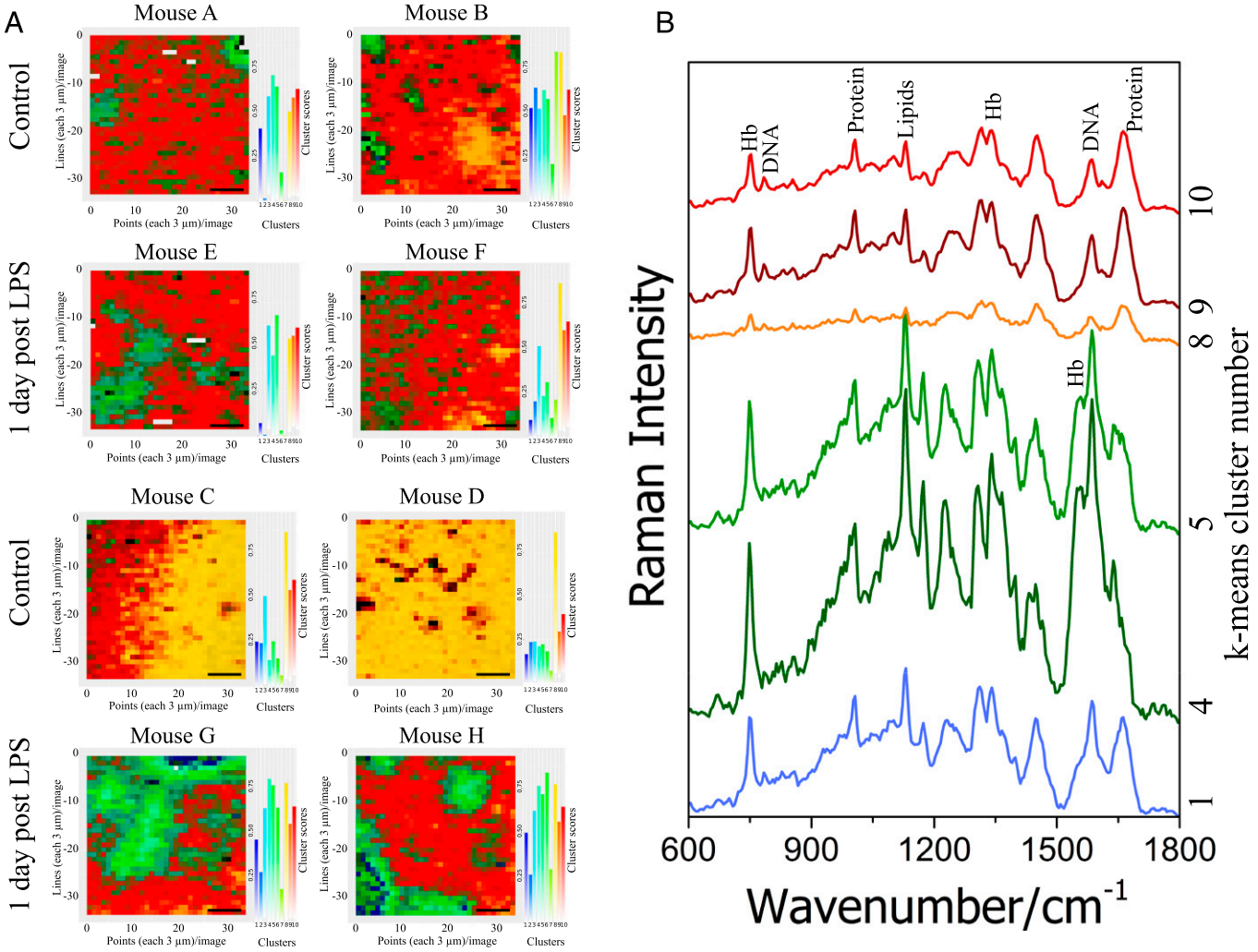

FIGURE 6. False-color Raman images of spleen tissue sections from control and LPS-treated animals obtained by *k*-means cluster analysis. (**A**) Representative Raman false-color images of spleen tissue sections from control mice (four animals, mouse A, B, C, and D) and LPS-treated mice (four animals, mouse E, F, G, and H) obtained by *k*-means cluster analysis. The x-axis and y-axis show step size (3 μm) used for Raman imaging. The spectra were processed to remove cosmic spikes and background corrected using SNIP algorithm. Raman fingerprint region (600 cm^{-1} to 1800 cm^{-1}) has been used for analysis. The *k*-means algorithm was executed to find ten different clusters of spectra from control and LPS-treated animals. The contribution of each cluster as cluster scores has been represented on right side of the individual tissue sections as cluster scores. (**B**) Corresponding Raman spectra of the clusters obtained from *k*-means analysis using the same color code as in (A). Spectra of clusters 1, 4, 5, 8, 9, and 10 are shown, whereas *k*-means cluster spectra 2, 3, 6, and 7 are omitted, as they correspond to individual image pixels with high fluorescence background that were registered on the spectrometer detector.

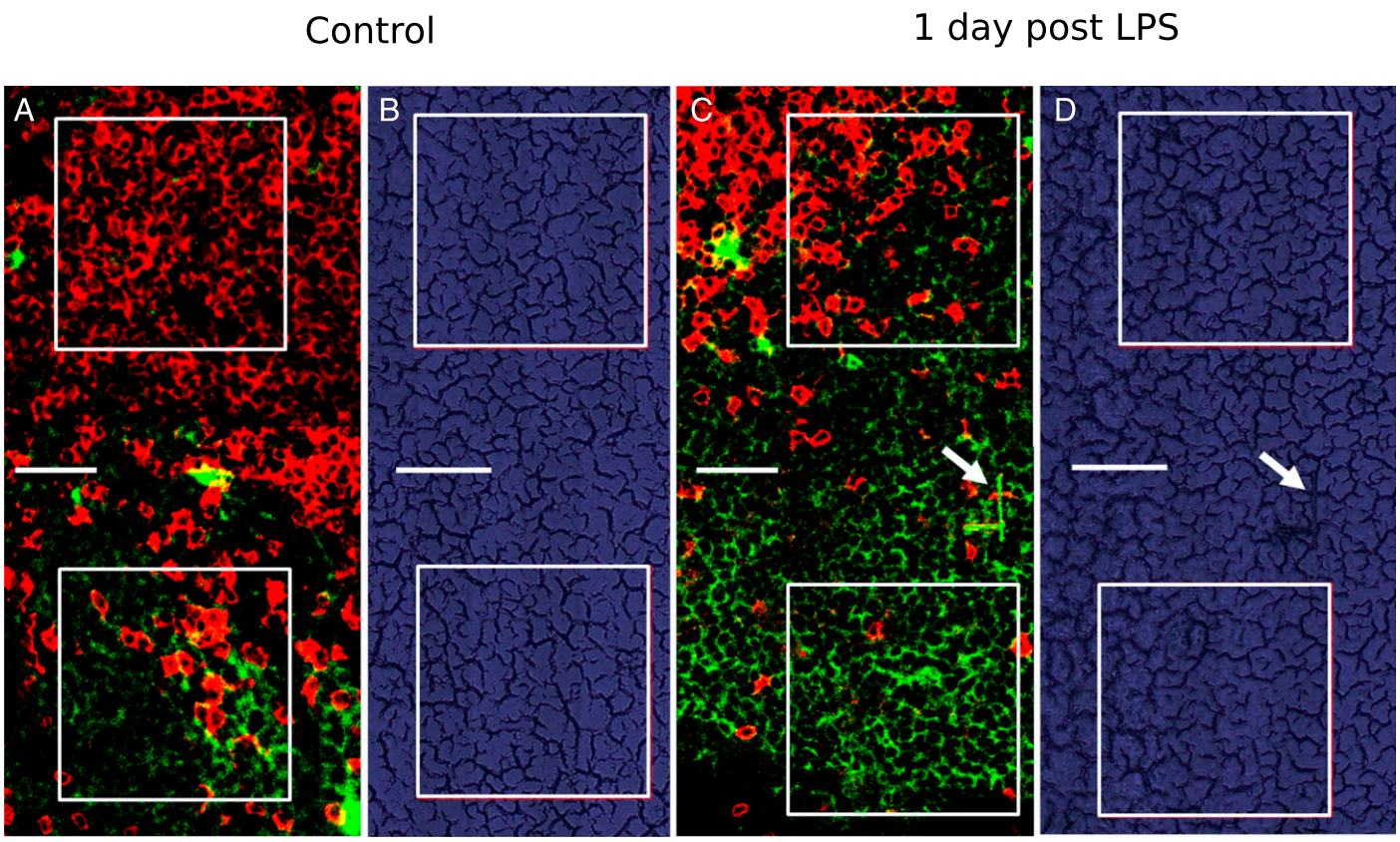

FIGURE 7. Fluorescence-stained images and respective bright-field images of mouse spleen tissue sections area investigated using Raman spectroscopy.

(**A**) Fluorescence-stained images (A and **C**) and bright-field images (**B** and **D**) of C57BL/6 mouse spleen cryosections of (A and B) sham mice treated with 0.9% saline water (C and D) 1 d post–LPS treatment. T cells were labeled with rat anti-CD3 Abs and detected using donkey anti-rat Alexa Fluor 555 (red color). B cells were labeled with donkey anti-mouse IgG Alexa Fluor 647 (green color). Images were collected using original magnification ×40 objective. Scale bar, 40 μm. The white squares represent regions scanned using Raman spectroscopy. The arrows indicate position of laser-induced mark on tissue section for correlation of the Raman-scanned region before and after fluorescence staining. Representative images from two sham mice and two LPS-treated mice from two separate biological experiments are shown.

Fig. 8 it can be visualized that higher numbers of T cells are present in the spleen of control mice, probably reflecting the previously reported acute loss of T cells in endotoxemia (1, 23, 31).

The relative ratio of T cells and B cells only for the tissue section regions where Raman mapping was carried out, the T cell number is reduced, and more B cells were observed in the LPS-treated mice as shown by the pie chart in Fig. 8B. The uneven distribution of T cells and B cells in the Raman-mapped regions might have an influence on the PCA-LDA model.

To inspect if the ratio of T cells and B cells influence the PCA-LDA model, Raman spectral features of T cells and B cells were extracted from the Raman-imaged area (guided by the fluorescence images) for control mice (Supplemental Fig. 3A, 3C) and LPS-treated mice (Supplemental Fig. 3B, 3D). Mean Raman spectra of T cells and B cells for a control and LPS-treated mice are shown in Supplemental Fig. 3E. Raman spectral profile of T cells from control mice spleen is different from the one of LPS-treated mice, whereas spectral variations are hardly observed for B cells in the spleen between control and LPS-treated mice, as observed in the Raman difference spectra (Supplemental Fig. 3F). Further, pairwise PCA-LDA was carried out between control mouse (named A, B, C, D) and LPS-treated mouse (named E, F, G, H), and the table of accuracy is shown in Table II. Irrespective of the heterogeneity in the T cell and B cell numbers, control mice could be differentiated from the LPS-treated mice with high accuracy. The accuracy between LPS-treated mouse F and control mice B and C reduces slightly (~68% accuracy); possibly the control mice are more ill, or vice-versa the LPS-treated mouse is still doing better than the other subjects from the treated group. These results indicate that the differences observed between control mice spleen and spleen from LPS-treated mice arise mainly because of T cells, with some contribution from the other players present in the spleen tissue.

DISCUSSION

This study demonstrates the suitability of Raman spectroscopy to follow changes associated to systemic inflammation within splenocytes.

https://doi.org/10.4049/immunohorizons.1800059

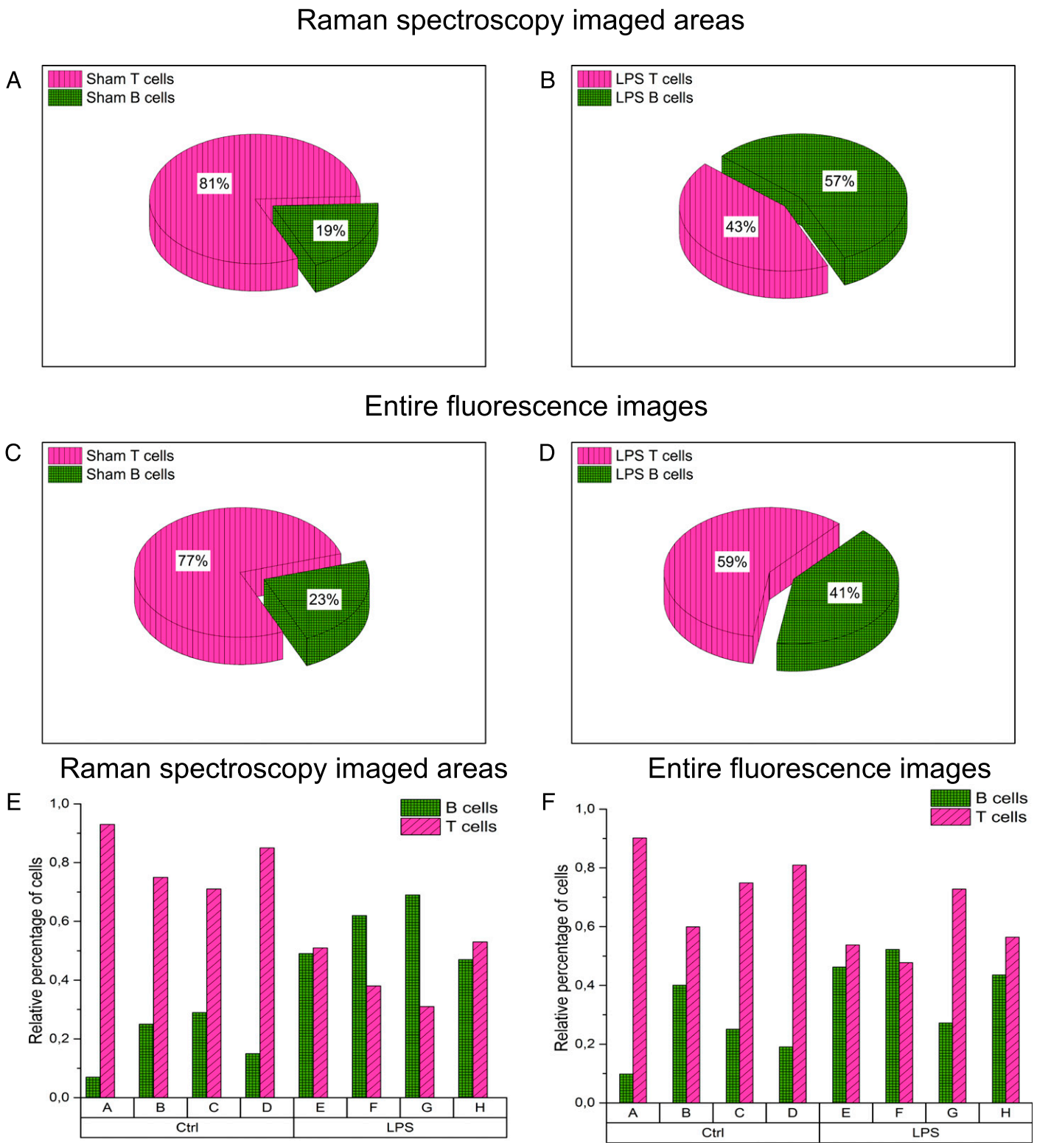

FIGURE 8. Pie charts (for all the mice together) and bar graph (for individual mouse) showing relative percentage of T cells and B cells present in the Raman spectroscopy–investigated area and entire fluorescence images of spleen from C57BL/6 mice spleen tissue sections.

Pie chart showing ratio of T cells and B cells present in the investigated spleen tissue sections, (**A**) in sham mice only from the Raman spectroscopic–imaged regions, (**B**) in LPS-treated mice only from the Raman spectroscopic–imaged regions, (**C**) in sham mice from entire fluorescence images, and (**D**) in LPS-treated mice from entire fluorescence images. Bar graph presenting relative percentage of T cells **(Continued)**

TABLE II. Accuracy (given in %) obtained for two-class PCA-LDA model generated for control mice (A, B, C, D) and LPS-treated C57BL/6 mice (E, F, G, H)

Mice	E	F	G	H
A	88.73	84.91	93.17	91.48
B	80.00	67.97	85.53	68.10
C	90.05	68.19	84.41	88.07
D	83.76	74.59	89.03	77.51

Chemical reactions triggered by LPS within cells via specific receptors such as TLR 4 mediate cellular immune response, which in turn affects the body's physiological conditions such as increase in clinical severity by elevated heart rhythm, rise in body temperature, weight loss, and increased mortality rate. Much of these pathological effects are owed to the release of proinflammatory mediators and cytokines upon LPS stimulation. During the proinflammatory and postinflammatory stages, lymphocytes play an important role as a member of the adaptive immune system. The major source of lymphocytes is spleen, which plays a central role in fluidic management and forms a migratory route for the lymphocytes (3). Hence, spleen resident T cells allow investigating long-term effects of LPS on their functionality.

Special focus has been placed on the major subpopulation of the splenocytes (i.e., $CD4^+$ T cells and $CD8^+$ T cells. The immunological and functional aspects of T cells 10 d post–LPS treatment indicated T cell ensuing normal functionality (23, 31). Indeed, the T cells' cytokine responses, upregulation of activation markers, or proliferation were previously found to be similar to the controls at this late, postacute time point in endotoxemia (23). The findings presented in this study, based on label-free Raman spectroscopy, are fully in line with the results from immunophenotyping. In addition, Raman spectroscopy gave deeper insights for different cellular biomolecules and the variation they undergo upon LPS insult. For instance, DNA peak intensity was observed to be higher in the control T cells compared with the LPS-treated T cells. This can be due to the dense nucleus structure that is usually observed in naive T cells (48). Conversely, structural integrity of the nucleus loosens up in T cells from endotoxemia as the nuclear processes are switched on in responses to inflammation (e.g., via stimulation of the NF of activated T cells (48–51). This effect is observed up to 10 d post–LPS insult in both $CD4^+$ T cells and $CD8^+$ T cell populations. However, at day 30, no more differences are observed in the peak intensity of the nucleus band except for $CD8^+$ T cells, in which a slight difference is still visible in the Raman difference spectra (Fig. 3F). Higher nucleus activity in terms of chromatin remodeling, DNA expression, and changes in the transcription factors–NF, and increase in activator protein has been previously reported and is indicative of cellular adaptation after endotoxin shock–related cell activation (52, 53). $CD8^+$ T cells are known as late responders in the presence of inflammation. This is reflected in the Raman spectra 30 d post–LPS insult that feature Raman peaks arising from DNA. These changes observed in T cells have been attributed to genomic rearrangements, as such transformation affects the compactness of chromatin as reported by Chan et al. (33) and hence the variation in the nucleus Raman peak intensities (54). Further, to sustain the large changes in the nucleus, large numbers of proteins are required in the activated T cells compared with the naive cells. As a result, immune-specific transcription factors upregulating the T cells' surface glycoproteins (17, 55, 56) show major contributions in the Raman difference spectra apart from Raman peaks of nucleic acids (57).

Further changes in the difference Raman spectrum between cells from control and LPS-treated mice are mainly associated with overall lipids and carbohydrates (Raman bands in the spectral region 1400–1500 cm^{-1}). PCA-LDA indicates T cells undergo major intracellular chemical restructuring 4 d post–LPS treatment, and these chemical changes are visible for $CD4^+$ T cells up to 10 d after LPS insult in the surviving mice. However, 30 d post–LPS treatment, discrimination is not possible between cells from LPS-treated and control mice, indicating the cells regain their initial chemical compositions. This indicates that T cells start recovering their original functional status 10 d post–LPS treatment, which is in good agreement with previous results obtained by immunophenotyping (23). However, although the evaluated clinical severity scores return to normal range 10 d post–LPS treatment (23), some subtle differences in the disease index can still be observed between the control and LPS-treated mice as shown previously (23). This may explain the small differences, especially the vibrational bands arising from the contributions of proteins observed in the Raman difference spectra 30 d after LPS treatment.

As a further step to minimize sample handling and to characterize the organ itself, spleen tissue was directly subjected to Raman spectroscopic analysis. This analysis pointed to major differences in the amount of heme (Hb content) between control and endotoxemia mice (58, 59). Relative high-intensity Hb peaks in the spleen of control mice is expected, as normal spleen is composed of ~80% red pulp (60–62) consisting primarily of RBCs along with a fair amount of T cells (58). This was also noted in the color of spleen after isolation, spleens of LPS-treated mice appearing pale-red color, whereas spleen from control mice were deep red (data not shown). However, the general anemic conditions of the animals were recorded from blood hemogram and have been previously reported (see figure 1D of Ref. 23). Hence, the

and B cells present in the fluorescence images of individual mouse spleen tissue section, (**E**) only from the Raman spectroscopic–imaged regions, and (**F**) from all the fluorescence images. To evaluate changes in the proportion of B cells and T cells in the investigated mice, the ratio of the areas covered with the respective fluorescence marker was calculated. The biological experiments were repeated four times with one mouse per condition. Three tissue slices were investigated per spleen. Mouse of strain type C57BL/6 were investigated using confocal fluorescence microscopy.

https://doi.org/10.4049/immunohorizons.1800059

absence of prominent DNA phosphate backbone vibration contributions in the treated mice, as observed from the LD loading, points in the direction of internucleosomal DNA cleavage of the apoptotic cells present in the tissue (51, 54, 63). The bright-field spleen tissue images of the LPS-treated mice in comparison with the control show scarring and tissue injury (Fig. 7B, 7D). These observed morphological changes in the spleen have been reported as a result of LPS insult (64), and it is also known that cleaved caspase-3–positive cells significantly increase in numbers after the LPS exposure causing widespread leukocyte apoptosis in the spleen tissue (65). The tissue injury hypothesis can be further confirmed with the presence of Raman vibrations arising from the cytochrome-c/heme moiety and is in accordance with reported studies in literature where presence of cytochrome and heme during tissue injury in organs such as brain has been observed (38, 66, 67). The *k*-means clustering image captures to some extent the contributions of DNA and heme. However, the spatial resolution used for Raman imaging of spleen tissue (3 μm) is not sufficient to reveal changes on cellular level.

The spleen harbors other resident splenocytes besides T cells, such as B cells, dendritic cells, or macrophages. Raman spectra of the tissue have contributions from various splenocytes and can influence the outcome of the PCA-LDA model. It has been previously reported that Raman spectroscopy is capable of differentiating between T cells and B cells (57). Because the tissue areas for Raman mapping were selected randomly, the possibility of uneven distribution of the T cells and B cells within the Raman-mapped area can be foreseen. The B cell spectra hardly show any difference between control and LPS-treated mice. However, the difference in the ratio of T cells to B cells might have an influence on the Raman model. One probable explanation is that similar to T cells, the B cells are not directly engaged by the LPS. Moreover, the precise mechanisms of lymphocyte homing or trafficking through the spleen during systemic inflammation are currently debated (3, 11, 68). In the current study, we consistently observed a severe drop in the number of splenic lymphocytes following the LPS challenge. This indicates that T cells transit from the spleen probably into lymphoid circulation. Alternatively, the decrease in lymphocyte numbers might reflect in situ apoptosis, although we did not obtain any proof of wide-spread splenocyte death in our experiments.

The accuracy of the PCA-LDA model increases when Raman spectra of an individual mouse from the control and the LPS-treated group were analyzed pairwise. The PCA-LDA accuracy table further shows the impact of the heterogeneity with which each mouse reacts to LPS (Table II). The accuracy to differentiate individual mice spleen of treated and untreated mice lays around 80–90%. The major spectral differences responsible for the differentiation of spleen tissue after LPS treatment arise because of the changes in the T cells cellular profile and the connective tissue structures of spleen itself. The spleen tissue is injured once inflammation is induced by administration of the LPS (66, 67). Indeed, being a central lymphoid organ, major changes in spleen architecture and cellularity can be easily observed in an infection scenario (2, 69). Thus, inflammation triggers cellular redistribution within the spleen (65), extensive cytokine production (69), and tissue scarring (3). Analysis of the spleen tissue in a label-free manner via Raman spectroscopy offers new possibilities for the noninvasive analysis and description of the immunological changes involved in the host response to systemic inflammation and sepsis.

The advantages of this new method are that it is unbiased as being label free and is a nondestructive technique, as samples are available after Raman measurements for immunohistochemistry analysis. Further, it has also shown the possibility to directly apply Raman spectroscopy for spleen tissue analysis. After Raman spectroscopic analysis, the tissue can still be used for classical immunofluorescence staining and analysis.

CONCLUSIONS

In this study, we demonstrate the possibility of using Raman spectroscopy to follow the T cell activation process post–LPS treatment in a rodent model of endotoxemia. The cells were analyzed from acute to postacute inflammation stages. Raman spectroscopy results indicate T cells gain back their major biochemical composition after LPS shock in the time spam of 30 d. Spleen tissue analysis of LPS-treated mice using Raman spectroscopy shows changes in Hb and DNA content. Fluorescence image analysis reveals higher number of B cells and reduced number of T cells in the spleen after LPS treatment. As a label-free method, Raman spectroscopy shows high potential for phenotyping of immune cells and following the dynamics of cellular activation response to endotoxins such as LPS.

DISCLOSURES

The authors have no financial conflicts of interest.

REFERENCES

1. Santana, C. C., J. Vassallo, L. A. de Freitas, G. G. Oliveira, L. C. Pontes-de-Carvalho, and W. L. dos-Santos. 2008. Inflammation and structural changes of splenic lymphoid tissue in visceral leishmaniasis: a study on naturally infected dogs. *Parasite Immunol.* 30: 515–524.
2. Gorąca, A., H. Huk-Kolega, P. Kleniewska, A. Piechota-Polańczyk, and B. Skibska. 2013. Effects of lipoic acid on spleen oxidative stress after LPS administration. *Pharmacol. Rep.* 65: 179–186.
3. Steiniger, B. S. 2015. Human spleen microanatomy: why mice do not suffice. *Immunology* 145: 334–346.
4. Pennock, N. D., J. T. White, E. W. Cross, E. E. Cheney, B. A. Tamburini, and R. M. Kedl. 2013. T cell responses: naive to memory and everything in between. *Adv. Physiol. Educ.* 37: 273–283.
5. McAleer, J. P., and A. T. Vella. 2008. Understanding how lipopolysaccharide impacts CD4 T-cell immunity. *Crit. Rev. Immunol.* 28: 281–299.
6. Rimmelé, T., D. Payen, V. Cantaluppi, J. Marshall, H. Gomez, A. Gomez, P. Murray, and J. A. Kellum, ADQI XIV Workgroup. 2016. Immune cell phenotype and function in sepsis. *Shock* 45: 282–291.
7. Hinds, P. W., S. F. Dowdy, E. N. Eaton, A. Arnold, and R. A. Weinberg. 1994. Function of a human cyclin gene as an oncogene. *Proc. Natl. Acad. Sci. USA* 91: 709–713.

8. Schwartz, R. H. 2003. T cell anergy. *Annu. Rev. Immunol.* 21: 305–334.
9. Unsinger, J., J. M. Herndon, C. G. Davis, J. T. Muenzer, R. S. Hotchkiss, and T. A. Ferguson. 2006. The role of TCR engagement and activation-induced cell death in sepsis-induced T cell apoptosis. *J. Immunol.* 177: 7968–7973.
10. Yi, J. S., M. A. Cox, and A. J. Zajac. 2010. T-cell exhaustion: characteristics, causes and conversion. *Immunology* 129: 474–481.
11. Poujol, F., G. Monneret, A. Pachot, J. Textoris, and F. Venet. 2015. Altered T lymphocyte proliferation upon lipopolysaccharide challenge ex vivo. *PLoS One* 10: e0144375.
12. Nutt, S. L., and J. R. Groom. 2018. Editorial overview: Lymphocyte development and activation. *Curr. Opin. Immunol.* 51: iv–vi.
13. Tinsley, K. W., M. H. Grayson, P. E. Swanson, A. M. Drewry, K. C. Chang, I. E. Karl, and R. S. Hotchkiss. 2003. Sepsis induces apoptosis and profound depletion of splenic interdigitating and follicular dendritic cells. *J. Immunol.* 171: 909–914.
14. Dannhauser, D., D. Rossi, P. Memmolo, F. Causa, A. Finizio, P. Ferraro, and P. A. Netti. 2017. Label-free analysis of mononuclear human blood cells in microfluidic flow by coherent imaging tools. *J. Biophotonics* 10: 683–689.
15. Mannie, M. D., T. J. McConnell, C. Xie, and Y. Q. Li. 2005. Activation-dependent phases of T cells distinguished by use of optical tweezers and near infrared Raman spectroscopy. *J. Immunol. Methods* 297: 53–60.
16. Neugebauer, U., J. H. Clement, T. Bocklitz, C. Krafft, and J. Popp. 2010. Identification and differentiation of single cells from peripheral blood by Raman spectroscopic imaging. *J. Biophotonics* 3: 579–587.
17. Brown, K. L., O. Y. Palyvoda, J. S. Thakur, S. L. Nehlsen-Cannarella, O. R. Fagoaga, S. A. Gruber, and G. W. Auner. 2009. Raman spectroscopic differentiation of activated versus non-activated T lymphocytes: an in vitro study of an acute allograft rejection model. *J. Immunol. Methods* 340: 48–54.
18. Schie, I. W., L. Alber, A. L. Gryshuk, and J. W. Chan. 2014. Investigating drug induced changes in single, living lymphocytes based on Raman micro-spectroscopy. *Analyst* 139: 2726–2733.
19. McNerney, G. P., W. Hübner, B. K. Chen, and T. Huser. 2010. Manipulating CD4+ T cells by optical tweezers for the initiation of cell-cell transfer of HIV-1. *J. Biophotonics* 3: 216–223.
20. Ramoji, A., U. Neugebauer, T. Bocklitz, M. Foerster, M. Kiehntopf, M. Bauer, and J. Popp. 2012. Toward a spectroscopic hemogram: Raman spectroscopic differentiation of the two most abundant leukocytes from peripheral blood. *Anal. Chem.* 84: 5335–5342.
21. Hobro, A. J., Y. Kumagai, S. Akira, and N. I. Smith. 2016. Raman spectroscopy as a tool for label-free lymphocyte cell line discrimination. *Analyst* 141: 3756–3764.
22. Schie, I. W., J. Rüger, A. S. Mondol, A. Ramoji, U. Neugebauer, C. Krafft, and J. Popp. 2018. High-throughput screening Raman spectroscopy platform for label-free cellomics. *Anal. Chem.* 90: 2023–2030.
23. Markwart, R., S. A. Condotta, R. P. Requardt, F. Borken, K. Schubert, C. Weigel, M. Bauer, T. S. Griffith, M. Förster, F. M. Brunkhorst, et al. 2014. Immunosuppression after sepsis: systemic inflammation and sepsis induce a loss of naïve T-cells but no enduring cell-autonomous defects in T-cell function. *PLoS One* 9: e115094.
24. Hobro, A. J., and N. I. Smith. 2017. An evaluation of fixation methods: spatial and compositional cellular changes observed by Raman imaging. *Vib. Spectrosc.* 91: 31–45.
25. Butler, H. J., L. Ashton, B. Bird, G. Cinque, K. Curtis, J. Dorney, K. Esmonde-White, N. J. Fullwood, B. Gardner, P. L. Martin-Hirsch, et al. 2016. Using Raman spectroscopy to characterize biological materials. *Nat. Protoc.* 11: 664–687.
26. Team, R. D. C. 2008. *R: A Language and Environment for Statistical Computing*. . R Foundation for Statistical Computing, Vienna, Austria.
27. Ryan, C. G., E. Clayton, W. L. Griffin, S. H. Sie, and D. R. Cousens. 1988. SNIP, a statistics-sensitive background treatment for the quantitative analysis of pixe spectra in geoscience applications. *Nucl. Instrum. Methods Phys. Res. B* 34: 396–402.
28. Bocklitz, T. W., T. Dörfer, R. Heinke, M. Schmitt, and J. Popp. 2015. Spectrometer calibration protocol for Raman spectra recorded with different excitation wavelengths. *Spectrochim. Acta A Mol. Biomol. Spectrosc.* 149: 544–549.
29. Eilers, P. H., and H. F. Boelens. 2005. Baseline correction with asymmetric least squares smoothing. Leiden University Medical Centre Report. Available at: https://zanran_storage.s3.amazonaws.com/www.science.uva.nl/ContentPages/443199618.pdf.
30. Schindelin, J., I. Arganda-Carreras, E. Frise, V. Kaynig, M. Longair, T. Pietzsch, S. Preibisch, C. Rueden, S. Saalfeld, B. Schmid, et al. 2012. Fiji: an open-source platform for biological-image analysis. *Nat. Methods* 9: 676–682.
31. Wang, Z., G. Luo, Y. Feng, L. Zheng, H. Liu, Y. Liang, Z. Liu, P. Shao, M. Berggren-Söderlund, X. Zhang, and N. Xu. 2015. Decreased splenic CD4(+) T-lymphocytes in apolipoprotein M gene deficient mice. *BioMed Res. Int.* 2015: 293512.
32. Recknagel, P., F. A. Gonnert, E. Halilbasic, M. Gajda, N. Jbeily, A. Lupp, I. Rubio, R. A. Claus, A. Kortgen, M. Trauner, M. Singer, and M. Bauer. 2013. Mechanisms and functional consequences of liver failure substantially differ between endotoxaemia and faecal peritonitis in rats. *Liver Int.* 33: 283–293.
33. Chan, J. W., D. S. Taylor, T. Zwerdling, S. M. Lane, K. Ihara, and T. Huser. 2006. Micro-Raman spectroscopy detects individual neoplastic and normal hematopoietic cells. *Biophys. J.* 90: 648–656.
34. Krafft, C., A. A. Ramoji, C. Bielecki, N. Vogler, T. Meyer, D. Akimov, P. Rösch, M. Schmitt, B. Dietzek, I. Petersen, et al. 2009. A comparative Raman and CARS imaging study of colon tissue. *J. Biophotonics* 2: 303–312.
35. Pijanka, J. K., N. Stone, A. V. Rutter, N. Forsyth, G. D. Sockalingum, Y. Yang, and J. Sulé-Suso. 2013. Identification of different subsets of lung cells using Raman microspectroscopy and whole cell nucleus isolation. *Analyst* 138: 5052–5058.
36. Ling, N. R. 1968. *Lymphocyte Stimulation*. . North-Holland Publishing Company, Amsterdam.
37. Davies, H. S., P. Singh, T. Deckert-Gaudig, V. Deckert, K. Rousseau, C. E. Ridley, S. E. Dowd, A. J. Doig, P. D. Pudney, D. J. Thornton, and E. W. Blanch. 2016. Secondary structure and glycosylation of mucus glycoproteins by Raman spectroscopies. *Anal. Chem.* 88: 11609–11615.
38. Ramoji, A., K. Galler, U. Glaser, T. Henkel, G. Mayer, J. Dellith, M. Bauer, J. Popp, and U. Neugebauer. 2016. Characterization of different substrates for Raman spectroscopic imaging of eukaryotic cells. *J. Raman Spectrosc.* 47: 773–786.
39. Wesełucha-Birczyńska, A., M. Kozicki, J. Czepiel, and M. Birczyńska. 2013. Raman micro-spectroscopy tracing human lymphocyte activation. *Analyst* 138: 7157–7163.
40. Galler, K., R. P. Requardt, U. Glaser, R. Markwart, T. Bocklitz, M. Bauer, J. Popp, and U. Neugebauer. 2016. Single cell analysis in native tissue: Quantification of the retinoid content of hepatic stellate cells. *Sci. Rep.* 6: 24155.
41. Tolstik, T., C. Marquardt, C. Beleites, C. Matthäus, C. Bielecki, M. Bürger, C. Krafft, O. Dirsch, U. Settmacher, J. Popp, and A. Stallmach. 2015. Classification and prediction of HCC tissues by Raman imaging with identification of fatty acids as potential lipid biomarkers. *J. Cancer Res. Clin. Oncol.* 141: 407–418.
42. Frame, L., J. Brewer, R. Lee, K. Faulds, and D. Graham. 2017. Development of a label-free Raman imaging technique for differentiation of malaria parasite infected from non-infected tissue. *Analyst* 143: 157–163.
43. den Hartigh, L. J., J. E. Connolly-Rohrbach, S. Fore, T. R. Huser, and J. C. Rutledge. 2010. Fatty acids from very low-density lipoprotein lipolysis products induce lipid droplet accumulation in human monocytes. *J. Immunol.* 184: 3927–3936.

44. Camerlingo, C., F. d'Apuzzo, V. Grassia, L. Perillo, and M. Lepore. 2014. Micro-Raman spectroscopy for monitoring changes in periodontal ligaments and gingival crevicular fluid. *Sensors (Basel)* 14: 22552–22563.
45. Neugebauer, U., S. H. Heinemann, M. Schmitt, and J. Popp. 2011. Combination of patch clamp and Raman spectroscopy for single-cell analysis. *Anal. Chem.* 83: 344–350.
46. Rygula, A., K. Majzner, K. M. Marzec, A. Kaczor, M. Pilarczyk, and M. Baranska. 2013. Raman spectroscopy of proteins: a review. *J. Raman Spectrosc.* 44: 1061–1076.
47. Galler, K., E. Fröhlich, A. Kortgen, M. Bauer, J. Popp, and U. Neugebauer. 2016. Hepatic cirrhosis and recovery as reflected by Raman spectroscopy: information revealed by statistical analysis might lead to a prognostic biomarker. *Anal. Bioanal. Chem.* 408: 8053–8063.
48. Schürmann, M., J. Scholze, P. Müller, J. Guck, and C. J. Chan. 2016. Cell nuclei have lower refractive index and mass density than cytoplasm. *J. Biophotonics* 9: 1068–1076.
49. Macian, F. 2005. NFAT proteins: key regulators of T-cell development and function. *Nat. Rev. Immunol.* 5: 472–484.
50. Rossol, M., H. Heine, U. Meusch, D. Quandt, C. Klein, M. J. Sweet, and S. Hauschildt. 2011. LPS-induced cytokine production in human monocytes and macrophages. *Crit. Rev. Immunol.* 31: 379–446.
51. Le Roux, K, L. C. Prinsloo, and D. Meyer. 2014. Metallodrug induced apoptotic cell death and survival attempts are characterizable by Raman spectroscopy. *Appl. Phys. Lett.* 105: 123702.
52. Cobb, J. P., R. S. Hotchkiss, I. E. Karl, and T. G. Buchman. 1996. Mechanisms of cell injury and death. *Br. J. Anaesth.* 77: 3–10.
53. Huber, R., R. Bikker, B. Welz, M. Christmann, and K. Brand. 2017. TNF tolerance in monocytes and macrophages: characteristics and molecular mechanisms. *J. Immunol. Res.* 2017: 9570129.
54. Rangan, S., S. Kamal, S. O. Konorov, H. G. Schulze, M. W. Blades, R. F. B. Turner, and J. M. Piret. 2018. Types of cell death and apoptotic stages in Chinese hamster ovary cells distinguished by Raman spectroscopy. *Biotechnol. Bioeng.* 115: 401–412.
55. Lund, P. J., J. E. Elias, and M. M. Davis. 2016. Global analysis of O-GlcNAc glycoproteins in activated human T cells. *J. Immunol.* 197: 3086–3098.
56. Andersson, L. C., C. G. Gahmberg, A. K. Kimura, and H. Wigzell. 1978. Activated human T lymphocytes display new surface glycoproteins. *Proc. Natl. Acad. Sci. USA* 75: 3455–3458.
57. Ichimura, T., L. D. Chiu, K. Fujita, H. Machiyama, T. Yamaguchi, T. M. Watanabe, and H. Fujita. 2016. Non-label immune cell state prediction using Raman spectroscopy. *Sci. Rep.* 6: 37562.
58. Willekens, F. L., B. Roerdinkholder-Stoelwinder, Y. A. Groenen-Döpp, H. J. Bos, G. J. Bosman, A. G. van den Bos, A. J. Verkleij, and J. M. Werre. 2003. Hemoglobin loss from erythrocytes in vivo results from spleen-facilitated vesiculation. *Blood* 101: 747–751.
59. Grover, G. J., and D. J. Loegering. 1982. Effect of splenic sequestration of erythrocytes on splenic clearance function and susceptibility to septic peritonitis. *Infect. Immun.* 36: 96–102.
60. Pochedly, C. E., H. R. Sills, and D. A. Schwartz. 1989. *Disorders of the Spleen: Pathophysiology and Management*. Marcel Dekker, New York, NY.
61. Huang, S., A. Amaladoss, M. Liu, H. Chen, R. Zhang, P. R. Preiser, M. Dao, and J. Han. 2014. In vivo splenic clearance correlates with in vitro deformability of red blood cells from plasmodium yoelii-infected mice. *Infect. Immun.* 82: 2532–2541.
62. Del Portillo, H. A., M. Ferrer, T. Brugat, L. Martin-Jaular, J. Langhorne, and M. V. Lacerda. 2012. The role of the spleen in malaria. *Cell. Microbiol.* 14: 343–355.
63. Brauchle, E., S. Thude, S. Y. Brucker, and K. Schenke-Layland. 2014. Cell death stages in single apoptotic and necrotic cells monitored by Raman microspectroscopy. *Sci. Rep.* 4: 4698.
64. Zhang, L. M., W. Song, H. Cui, L. Q. Xing, H. B. Du, Y. Cui, W. H. Chen, Z. G. Zhao, and C. Y. Niu. 2015. Normal mesenteric lymph ameliorates lipopolysaccharide challenge-induced spleen injury. *Acta Cir. Bras.* 30: 604–610.
65. Kuypers, E., M. G. M. Willems, R. K. Jellema, M. W. Kemp, J. P. Newnham, T. Delhaas, S. G. Kallapur, A. H. Jobe, T. G. A. M. Wolfs, and B. W. Kramer. 2015. Responses of the spleen to intraamniotic lipopolysaccharide exposure in fetal sheep. *Pediatr. Res.* 77: 29–35.
66. Tachtsidis, I., M. M. Tisdall, C. Pritchard, T. S. Leung, A. Ghosh, C. E. Elwell, and M. Smith. 2011. Analysis of the changes in the oxidation of brain tissue cytochrome-c-oxidase in traumatic brain injury patients during hypercapnoea: a broadband NIRS study. *Adv. Exp. Med. Biol.* 701: 9–14.
67. Sanderson, T. H., J. M. Wider, I. Lee, C. A. Reynolds, J. Liu, B. Lepore, R. Tousignant, M. J. Bukowski, H. Johnston, A. Fite, et al. 2018. Inhibitory modulation of cytochrome c oxidase activity with specific near-infrared light wavelengths attenuates brain ischemia/reperfusion injury. [Published erratum appears in 2018 *Sci. Rep.* 8: 6729.] *Sci. Rep.* 8: 3481.
68. Semaeva, E., O. Tenstad, J. Skavland, M. Enger, P. O. Iversen, B. T. Gjertsen, and H. Wiig. 2010. Access to the spleen microenvironment through lymph shows local cytokine production, increased cell flux, and altered signaling of immune cells during lipopolysaccharide-induced acute inflammation. *J. Immunol.* 184: 4547–4556.
69. Moehrlen, U., A. Lechner, M. Bäumel, K. Dostert, J. Röhrl, M. Meuli, D. N. Männel, and J. Hamacher. 2012. Immune cell populations and cytokine production in spleen and mesenteric lymph nodes after laparoscopic surgery versus conventional laparotomy in mice. *Pediatr. Surg. Int.* 28: 507–513.